Journal of Geophysical Research – Earth Surface

Supporting Information for

A model for oceanic melt rates under ice shelves using a balance-flux approach (CHICO)

David Pollard[1] and Robert M. DeConto[2]

1. Earth and Environmental Systems Institute, Pennsylvania State University, University Park, PA 16802, USA

2. Department of Geosciences, University of Massachusetts, Amherst, MA 01003, USA

Contents of this file

Introduction

- Section S1 contrasts modern results with a much simpler ocean-melt parameterization used in previous long-term ice-sheet modeling;
- Section S2 shows results using an alternate form of the non-dimensional distance metric as used in PICO and PICOP;
- Section S3 shows several other plume variables to illustrate model performance a general description of processing steps used;
- Section S4 describes an option to include additional seasonal melting near the ice edge;
- Section S5 tests results against numerical solutions of the basic differential equations for plume flow in 1-D flowline settings.

Section S1. Comparison with simple parameterization

Results are compared here with a much simpler parameterization of sub-ice ocean melt used in previous ice-sheet modeling (e.g., DeConto and Pollard, 2016), that depends only on the squared difference between the basal freezing point and the proximal open-ocean temperature (Holland et al., 2008)

$$\dot{m}_s = O_s \, K_s \left(T_o - T_f\right) \left|T_o - T_f\right| \tag{S1.1}$$

where $\dot{m}_s$ is sub-ice melt (m yr^{-1}), T_o is the proximal ocean water temperature (°C), T_f is the sea-water freezing point at the base of the ice (°C), K_s is a constant coefficient = 0.224 m yr^{-1} °C^{-2}, and O_s is a dimensionless $O(1)$ multiplier.

A set of runs was performed using the simple parameterization for continental Antarctica at 10 km resolution. As in the main paper, proximal open-ocean temperatures T_o were obtained from the WOA 2018 dataset (Boyer et al., 2018) and shifted to agree with shelf-edge averages in Reese et al. (2018). The multiplier O_s in Eq. (S1.1) was varied over all integer values from 1 to 30, and scores were calculated for each run using Eq. (12) as in the main paper. The optimal score was obtained with O_s = 14, which is used for the results in this Appendix (although O_s = 4 yielded the most realistic melt value averaged over all Antarctic shelf areas).

In Fig. S1.1 map results for the simple parameterization are compared with the two-layer model and with observed (Adusumilli et al., 2020), for the modern WAIS with grid resolution of 5 km. There is still little agreement with observed patterns of melt within individual ice shelves, both for the two-layer model and the simple parameterization. But the intra-shelf patterns for the simple parameterization (Fig. S1.1b) are quite different and correspond even less to those observed.

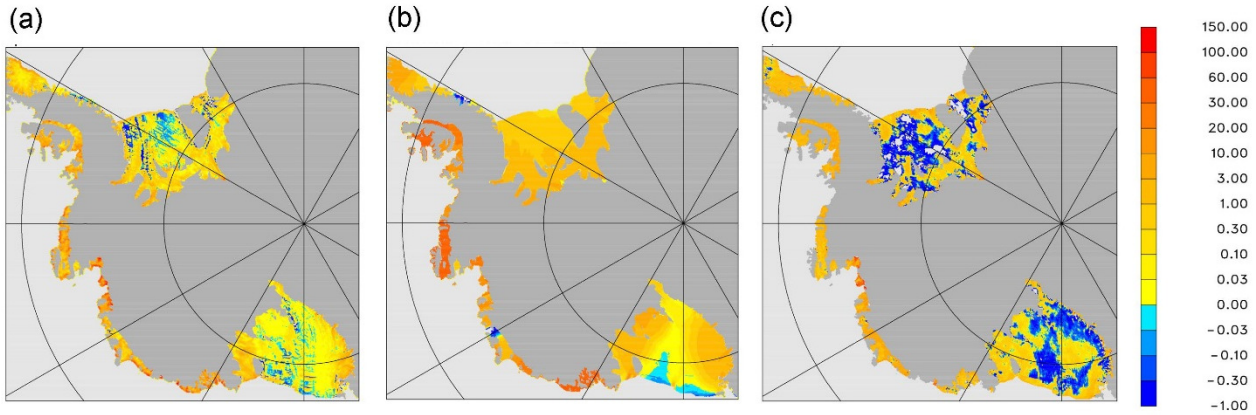

Figure S1.1. Oceanic melt rates (m yr^{-1} of ice) for West Antarctica (5 km grid**). (a)** Two-layer model. **(b)** Simple parameterization based on the squared difference between basal freezing point and proximal ocean temperature. **(c)** Observed, calculated from Adusumilli et al. (2020).

Fig. S1.2 shows shelf-average melt rates for the full set of shelves around Antarctica computed at 10 km resolution. For some shelves the model values are similar to each other and reasonably close to observed. However for the Ross and Filchner-Ronne (ROS, FIL) the simple parameterization values are too large, and for many smaller shelves they are considerably too small (DRY, NIN, MER, TOT, SHA, BAU, FIM). This is borne out by the score S (Eq. 12) which is 4.53 for the simple parameterization compared to 2.28 for the two-layer model, indicating that the simple parameterization is generally less realistic.

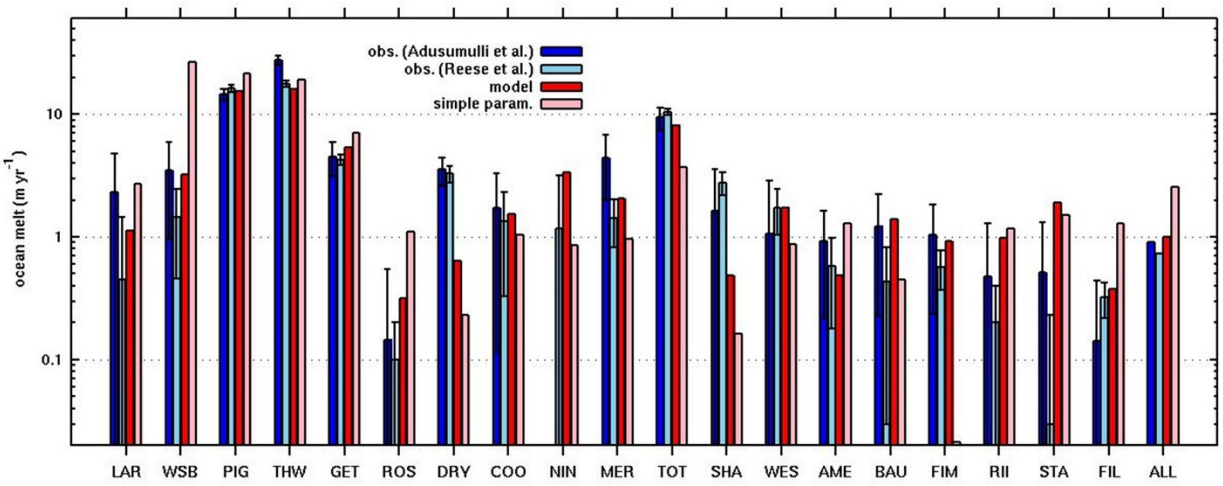

Figure S1.2. Average oceanic melt rates (m yr^{-1} of ice) for individual ice shelves (same set as in Reese et al., 2018; labels defined in Table 1, 10 km grid). **Dark blue:** Observed, calculated from Adusumilli et al. (2020). **Light blue:** Observed, from Reese et al. (2018) and Rignot et al. (2013). Whiskers show the uncertainty ranges given in those references. **Red:** Two-layer model. **Pink:** Simple parameterization.

Fig. S1.2 also shows observational values and ranges both from Adusumilli et al. (2020) and Reese et al. (2013). As discussed in the main text, there are significant differences between the two datasets for some shelves, comparable to some of the differences from the model values, and the reliability of observations may be a concern in more refined model evaluations.

Section S2. Alternate form of the non-dimensional distance metric

The form of the non-dimensional distance metric R in Eq. 9, representing the overall transition from ice-shelf edges to grounding lines, is an important component of the model. It is especially important in the balance-flux approach, as it explicitly determines the directions of horizontal flow in each layer. The goal in defining R is to yield broad-scale smooth patterns of ocean flow from the shelf edges through the shelf interior to the inner grounding lines (for the lower layer, and in reverse for the upper layer), adapting sensibly to 2-D basin shapes and diversions around interior islands such as Berkner Island in the Filchner-Ronne and Roosevelt Island in the Ross, but without introducing non-physical smaller-scale flows. The metric R used in the main paper (Eq. 9) yields reasonable results and partially achieves this goal; as described in the main text, this is only after additional smoothing of R (Eq. 10) to reduce "funneling" in the flow stemming from spatial irregularities in large ice-shelf edges (Ross and Filchner-Ronne) that would otherwise propagate as ridges and valleys into the interior and unrealistically concentrate the flow into narrow channels.

Other forms of R are possible, and here we compare results with another form replacing Eq. (9):

$$R = d_e / \left(d_e + d_g\right) \tag{S2.1}$$

where d_e and d_g are distances to the closest ice-shelf edge and grounding line respectively, calculated by nearest-neighbor iteration staying within the shelf as described in section 2.6. This is the same metric as used in PICO and PICOP (actually 1-R in those studies). R is 0 at all

ice-shelf edges, and 1 at all grounding lines. Exactly the same smoothing and infilling operations are then performed on *R* as described in section 2.6.

Modern results are shown in Fig. S2.1 for WAIS at 5 km grid resolution, and compared to observed (Adusumilli et al., 2020). There is little to choose between the magnitudes and patterns of melt rates, which are quite similar for the two model versions, with neither being obviously more realistic.

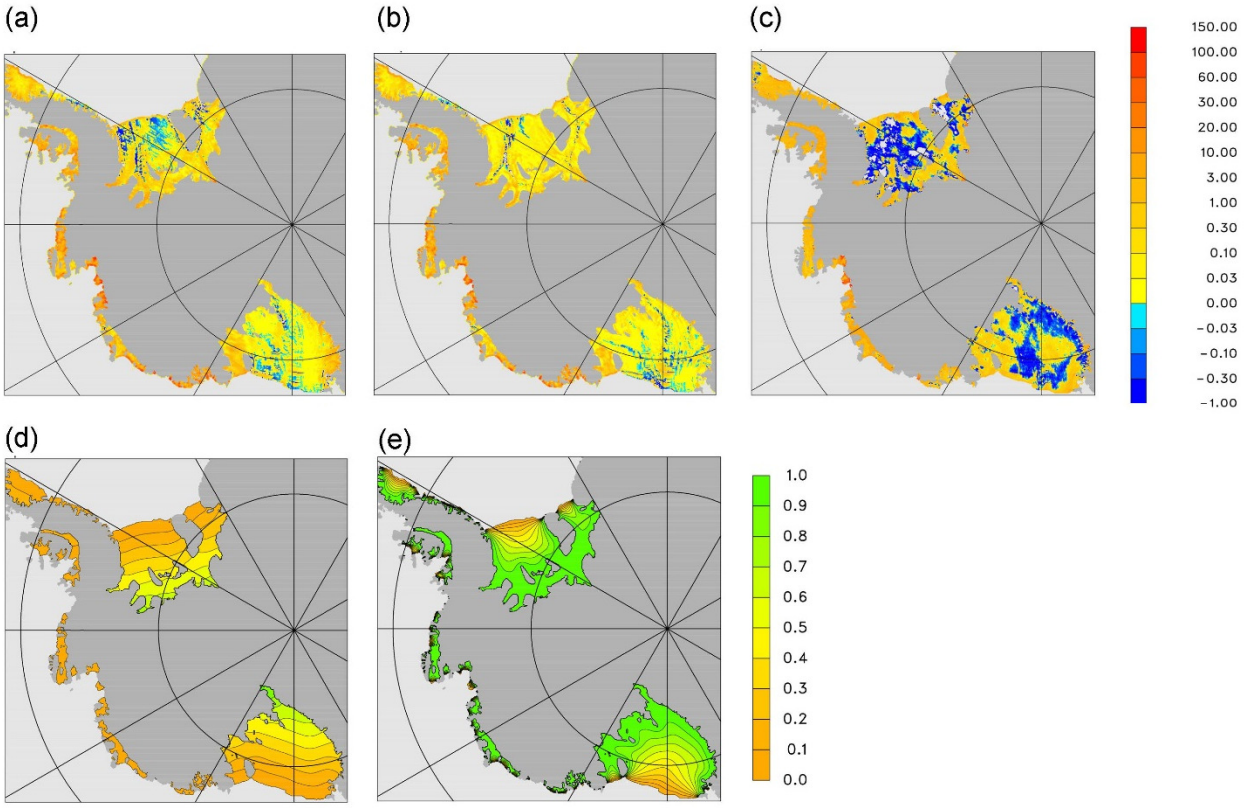

Figure S2.1. Oceanic melt rates (m yr^{-1} of ice) for West Antarctica (5 km grid), using different non-dimensional distance metrics *R*. **(a)** Model with standard *R* in Eq. 9. **(b)** Model with alternate *R* in Eq. S2.1. **(c)** Observed (Adusumilli et al., 2020). **(d)** *R* in Eq. 9, used for panel a. **(e)** *R* in Eq. S2.1, used for panel b.

The two distance metrics themselves are also shown in Fig. S2.1d,e. The main difference between them is the degree to which the flow "bends" around interior grounded islands. As expected, Eq. S2.1 produces greater deviation of the flow in the lee of the major islands grounded within the Ross and Filchner-Ronne shelves (Roosevelt, Berkner and others), causing greater curvature of flow behind them, but differences in the melt patterns in those regions are minor.

Section S3. Other plume variables

Several other variables of the main two-layer model are shown here to illustrate the working of the model. Modern results for the WAIS domain at 5 km resolution are used. Upper-layer

thickness (*D*) is shown in Fig. S3.1a. As expected, entrainment of lower-layer water into the upper layer causes a general thickening of the layer as it flows from grounding lines to edges under the large Filchner-Ronne and Ross shelves, from ~2 m to *O*(20) m. Melting from the ice base also contributes but is much smaller than entrainment.

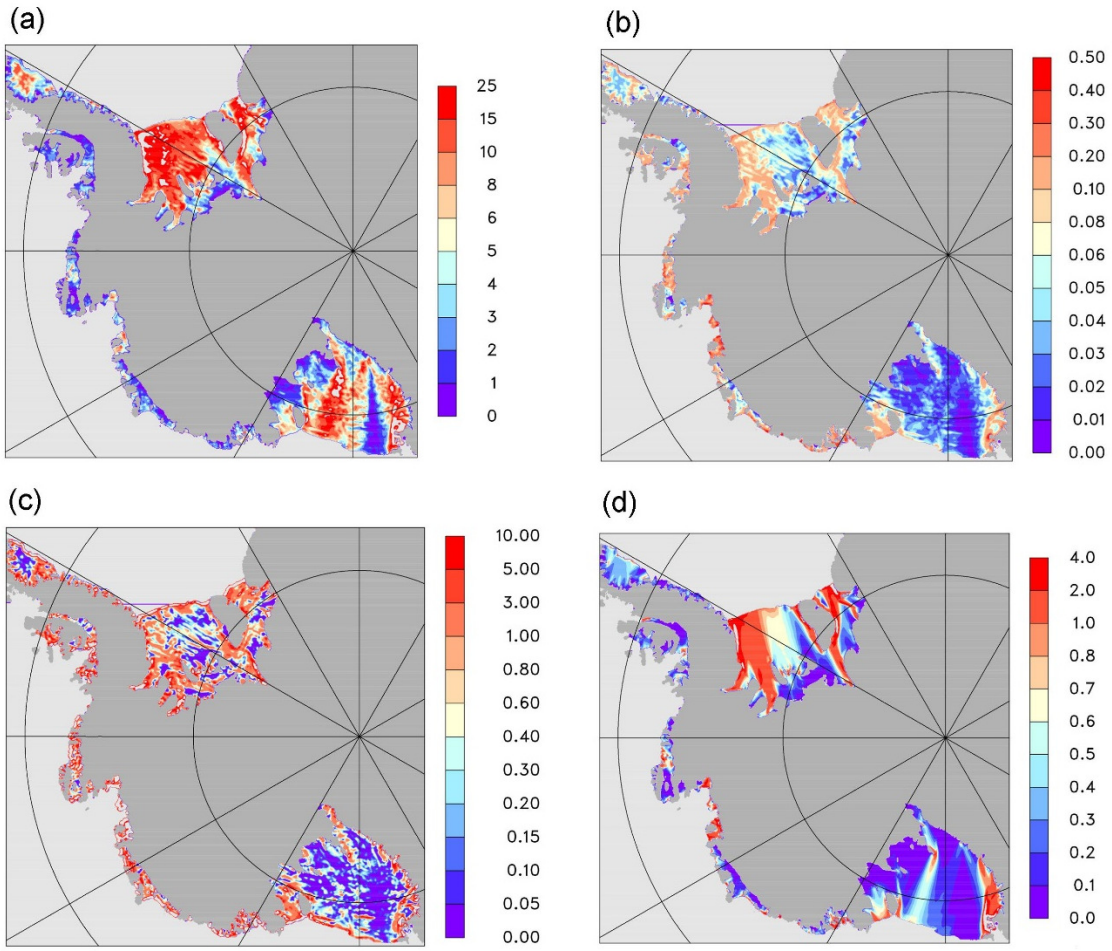

Figure S3.1. Other upper-layer plume variables in the two-layer model. **(a)** Layer thickness *D* (m)**. (b)** Plume velocity *U* (m s^{-1}). **(c)** Entrainment rate of lower-layer water into the upper layer $\dot{e}$ (10^{-6} m s^{-1}). **(d)** Mass flux per unit transverse length *F* (m^2 s^{-1}).

The patterns of the other variables are organized more into bands parallel to the outgoing flow, due in part to the blocking effects of the major grounded islands within the Ross and Filchner-Ronne shelves. Outward velocities (*U*, Fig. S3.1b) range from nearly 0 to a few 10's of cm s^{-1}. Entrainment rates ($\dot{e}$, Fig. S3.1c) range from ~0 to 10 x 10^{-6} m s^{-1}, with patterns generally following those of velocity as expected from Eq. 2. The outward mass flux per unit transverse length $F = D\,U$ (m^2 s^{-1}) is shown in Fig. S3.1d, strongly organized into along-flow bands.

The same four variables are shown in Fig. S3.2 using the alternate form of the non-dimensional distance metric *R* (Eq. S2.1, discussed in section S2). The general magnitudes are the same as those in Fig. S3.1 using the standard metric (Eq. 9), but here the banded structure parallel to the flow is considerably more prominent for all four variables. To some extent this is expected

because the alternate metric "bends" the flow around impediments such as grounded islands (Fig. S2.1e). Importantly, this banding is less prominent in the resulting ocean melt rates, whose patterns are similar to those with the standard metric (Fig. S2.1b vs. a). In further work, the choice of distance metric may be guided by comparing the quantities and patterns in Figs. S3.1 and S3.2 with high-resolution dynamical ocean model simulations.

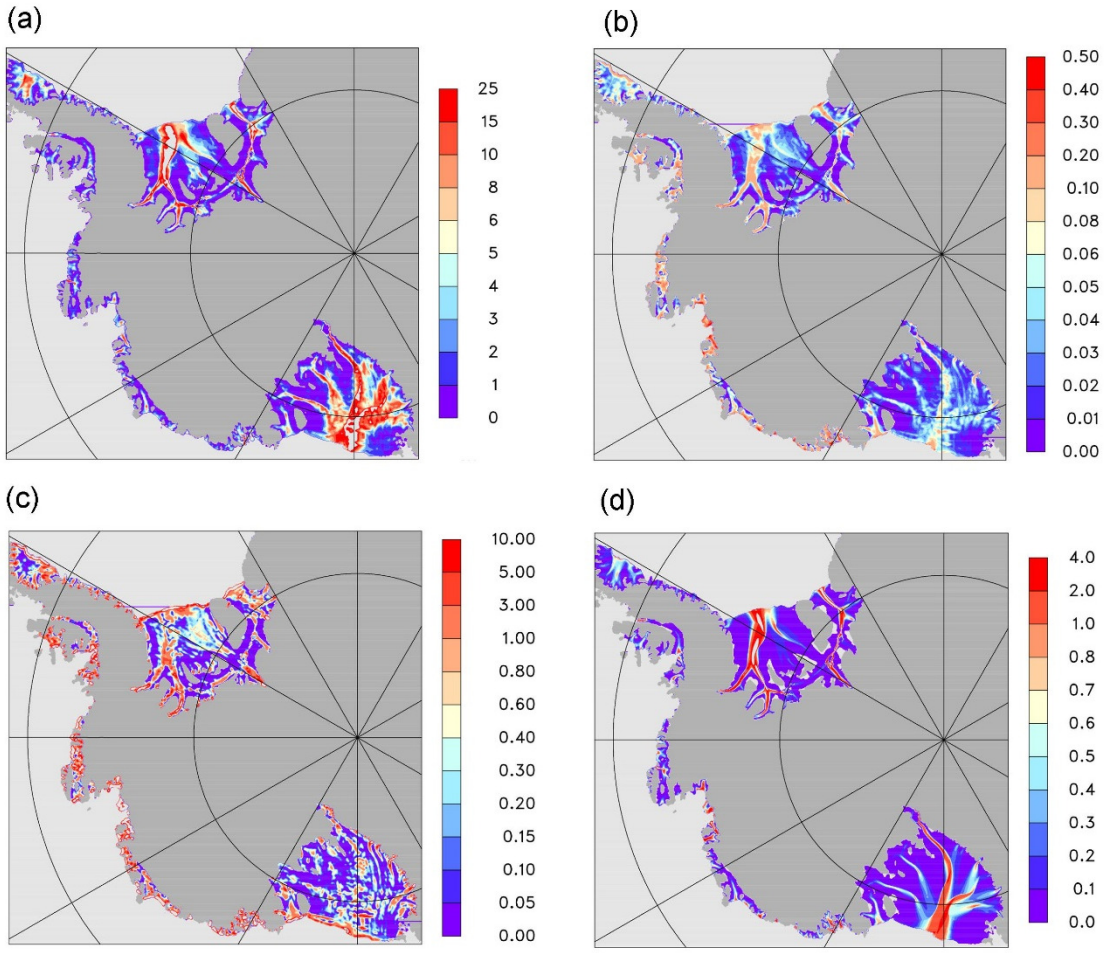

Figure S3.2. As Fig. S3.1 except with alternate form of non-dimensional metric R (Eq. S2.1).

Section S4. Antarctic Surface Water (AASW) melting

Incursion of seasonally warmed Antarctic surface water (AASW) under the ice shelf due to tides and other small-scale currents can cause melting near the edges (Mode 3 melting, Adusumilli et al., 2020). Bands of higher melting around the edges of the Ross, Filchner-Ronne and Amery shelves are arguably seen in observed maps (Adusumilli et al., 2020), and are more apparent in Pelle et al. (2019, their Fig. 2 for the Filcher-Ronne) and Moholdt et al. (2014, their Fig. 10 for the Ross and Filchner-Ronne).

This melting can be included simply in the model. First, AASW water temperatures (T_a) are obtained from the WOA 2018 database (Boyer et al., 2018) using their seasonal January-February-March average surface ocean temperatures. As for the T_o and S_o fields in section 2.8,

T_a is interpolated to the ice-model grid, extrapolated to ice-shelf edges where necessary, and smoothed by linear diffusion as in section 2.7. Then the AASW basal melt rate $\dot{m}_a$ (m yr^{-1} of ice) is given by

$$\dot{m}_a = A(T_a - T_f)w_a \qquad \text{(S4.1)}$$

where A = 0.5 m yr^{-1} C^{-1}. T_f is the ocean freezing point at the ice base, and the factor w_a represents limited spatial penetration beyond the shelf edge:

$$w_a = \max\,[\,0\,, 1 - d_e/10^5\,] \qquad \text{(S4.2)}$$

where d_e (m) is distance to the nearest ice-shelf edge calculated as described in section 2.6; w_a limits the AASW melting to the outermost 100 km of ice shelves. The ocean melt predicted by the model is set to the larger of $\dot{m}$ and $\dot{m}_a$ at each grid point (with the units of $\dot{m}$ from Eq. 3 converted from m s^{-1} of ocean water equivalent to m yr^{-1} of ice).

As seen in Fig. S4.1, the AASW mechanism produces higher melt rates (a few m yr^{-1}) in distinct bands ~100 km wide around the edges of the Ross and Filchner-Ronne shelves, similar to the bands suggested by observations mentioned above. This may be more important in future modeling work as patterns of simulated melt within individual ice sheets become more realistic.

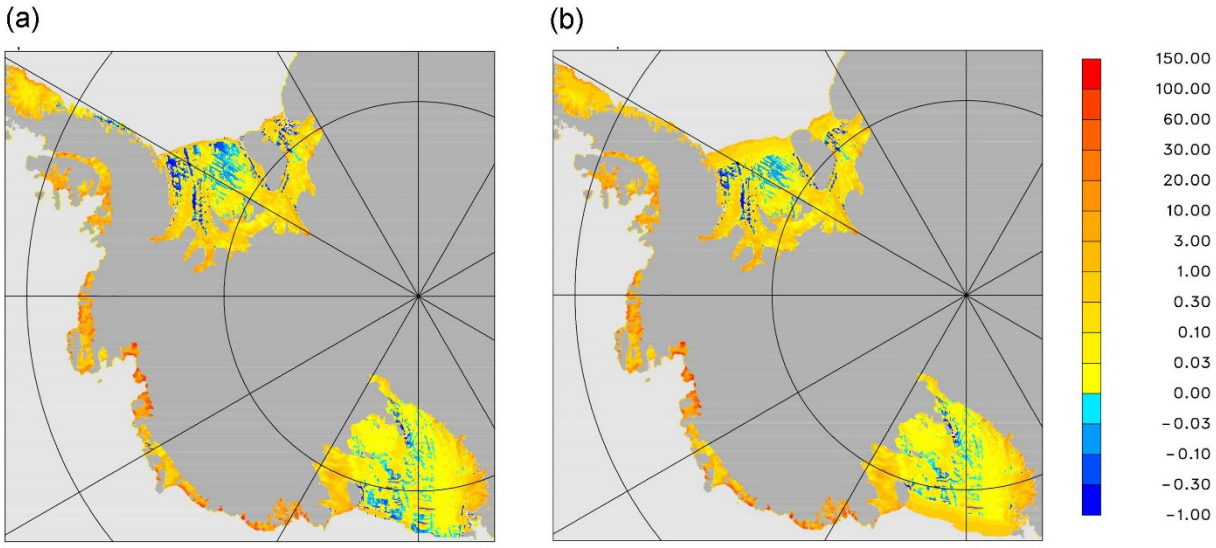

Figure S4.1. Oceanic melt rates (m yr^{-1} of ice) for West Antarctica (5 km grid). **(a)** Standard model (without AASW melting). **(b)** With additional melting by warm-season Antarctic Surface Water (AASW, Mode 3).

Section S5. Comparison with numerical plume solutions for 1-D flowlines

Our finite-differencing and method of solution for the balance-flux form of the dynamical equations (section 2.2., Eqs. 4) can be tested by comparing with numerical solutions of the basic plume equations (section 2.1, Eqs. 1), in 1-D flowline settings. Jenkins (1991, 2011)

similarly solved the basic plume equations (Eqs. 1) for various flowlines. Here we numerically solve Eqs. (1) and compare solutions with the balance-flux model in Eqs. (4).

To obtain stable numerical solutions of the plume equations (Eqs. 1), we found that several steps were needed: a predictor-corrector method, a staggered grid for velocity U shifted half a grid box from the main grid, upstream values for advected quantities, inclusion of $\partial/\partial t$ terms and temporal integration to equilibrium, and a short time step (.001 days with 0.2 km grid size). The resulting finite-difference scheme is quite different from that described in section 2.2 for Eqs. (4).

Solutions are first compared for an idealized ice-shelf profile with thickness h given by

$$h = h_{gl} - \left(\frac{1 - e^{-\frac{3x}{L}}}{1 - e^{-3}} \right) \left(h_{gl} - h_{ed} \right) \qquad \text{(S5.1)}$$

where $h_{gl} = (\rho_w/\rho_i)$ x 1000 m is ice thickness at the grounding line, h_{ed} = 100 m is ice thickness at the ice edge, L = 140 km is the ice-shelf length, and x is distance downstream from the grounding line. The grid size is 1 km for the balance-flux model and 0.2 km for the basic equations.

Fig. S5.1 shows the main variables for the two solutions. The left-hand column is for a warmer ocean, with ocean temperature T_o = 0 °C and salinity S_o = 34.5 ‰ at the edge of the shelf (and everywhere below the plume layer). The right-hand column is for a cooler ocean with T_o = -1.7 °C and S_o = 34.5 ‰. In both cases there is stronger melting near the grounding line as expected due to lower freezing points at depth and so greater difference with plume temperatures (Fig. S5.1o,p). The cooler ocean produces freeze-on under the outer half of the shelf (Fig. S5.1p). The largest discrepancies from the basic-equations solution occur for T and S (and hence $\Delta\rho$) in the first few km from the grounding line, as might be expected because of the steep gradients and proximity to the boundary. However, these differences in T and S are still quite small compared to the contrasts with the lower-layer values (0 or -1.7 °C, 34.5 ‰) rapidly being entrained into the plume.

The balance-flux results agree closely with the basic-equations. Even the largest differences are relatively small at the scales and magnitudes of interest in the Antarctic model applications of this paper. This is still true for coarser resolutions in the balance-flux model, for which melt rates are shown by symbols in Fig. S5.1o,p (which benefit from the slight modification to finite differencing for cells adjacent to the grounding line, described in section 2.3); the main effect of the coarser resolutions is to shift the high-melt region away from the grounding line by ~ 1 grid cell. We consider that the level of agreement between the two solutions in Fig. S5.1 is a good validation of our balance-flux equations and method of solution (Eqs. 4, sections 2.2 to 2.4).

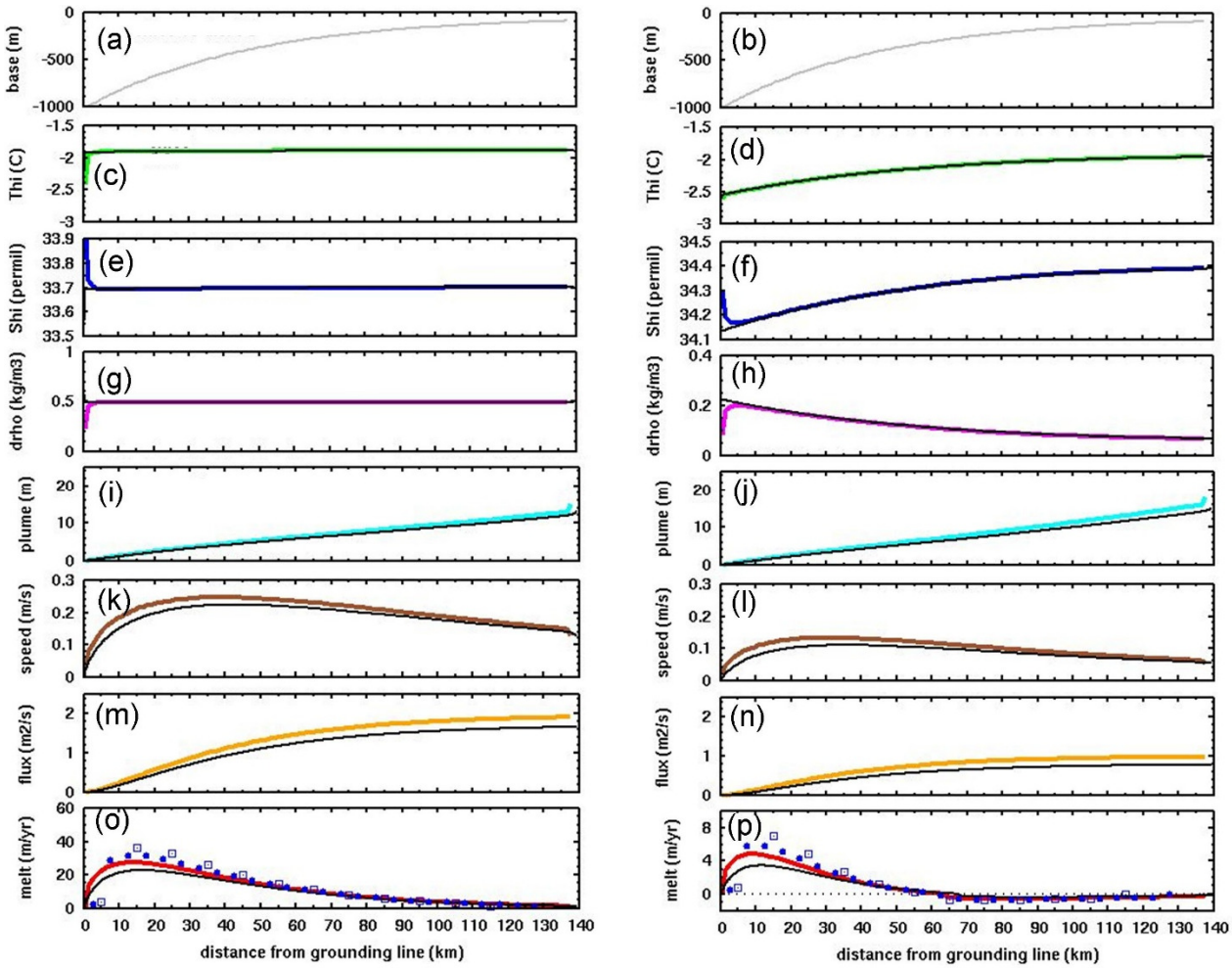

Figure S5.1. Upper-layer plume variables in simulations for an idealized 1-D ice shelf profile. Thick colored lines are for the balance-flux model with grid resolution 1 km (Eqs. 4), and black lines are numerical solutions of the basic plume equations with grid resolution 0.2 km. (Eqs. 1). The x axis is horizontal distance (km) from the grounding line at x = 0 (+ one cell width) to the ice-shelf edge at x = 140 km. **Left column:** oceanic (and lower-layer) temperature and salinity are T_o = 0 °C, S_o = 34.5 ‰. **Right column:** T_o = -1.7 °C, S_o = 34.5 ‰. Note the different y-scales for some of the variables. **(a,b)** Depth of ice-shelf base (m, grey line). **(c,d)** Temperature T (°C). **(e,f)** Salinity S (‰). **(g,h)** Density difference $\Delta\rho$, lower minus upper layer (kg m^{-3}). **(i,j)** Layer thickness D (m). **(k,l)** Velocity U (m s^{-1}). **(m,n)** Mass flux F (m^2 s^{-1}). **(o,p)** Sub-ice oceanic melt rate (m yr^{-1} of ice). Blue symbols in panels o and p show model melt rates for coarser grid resolutions of 5 km (solid dots) and 10 km (hollow squares).

Fig. S5.2 shows solutions for a profile representing the modern Pine Island Glacier ice shelf, running from grounding line to shelf edge. The basal ice depth (Fig. S5.2a) is derived from Bedmachine (Morlighem, 2020; Morlighem et al., 2020), aggregated to our 2 km grid as in the 2-D ASE simulations shown in the main paper. Both the balance-flux model and basic-equations solution use a grid size of 2 km for the flowline here. Proximal ocean (and lower-layer) temperature T_o = 0.46 °C and salinity S_o = 34.55 ‰ are prescribed as in Table 1 and Reese et al. (2018). The left-hand column is with the unsmoothed ice-shelf profile, and the right-hand

column is with diffusive spatial smoothing applied to basal slopes sin α for a duration of 0.1 years (Eq. 11).

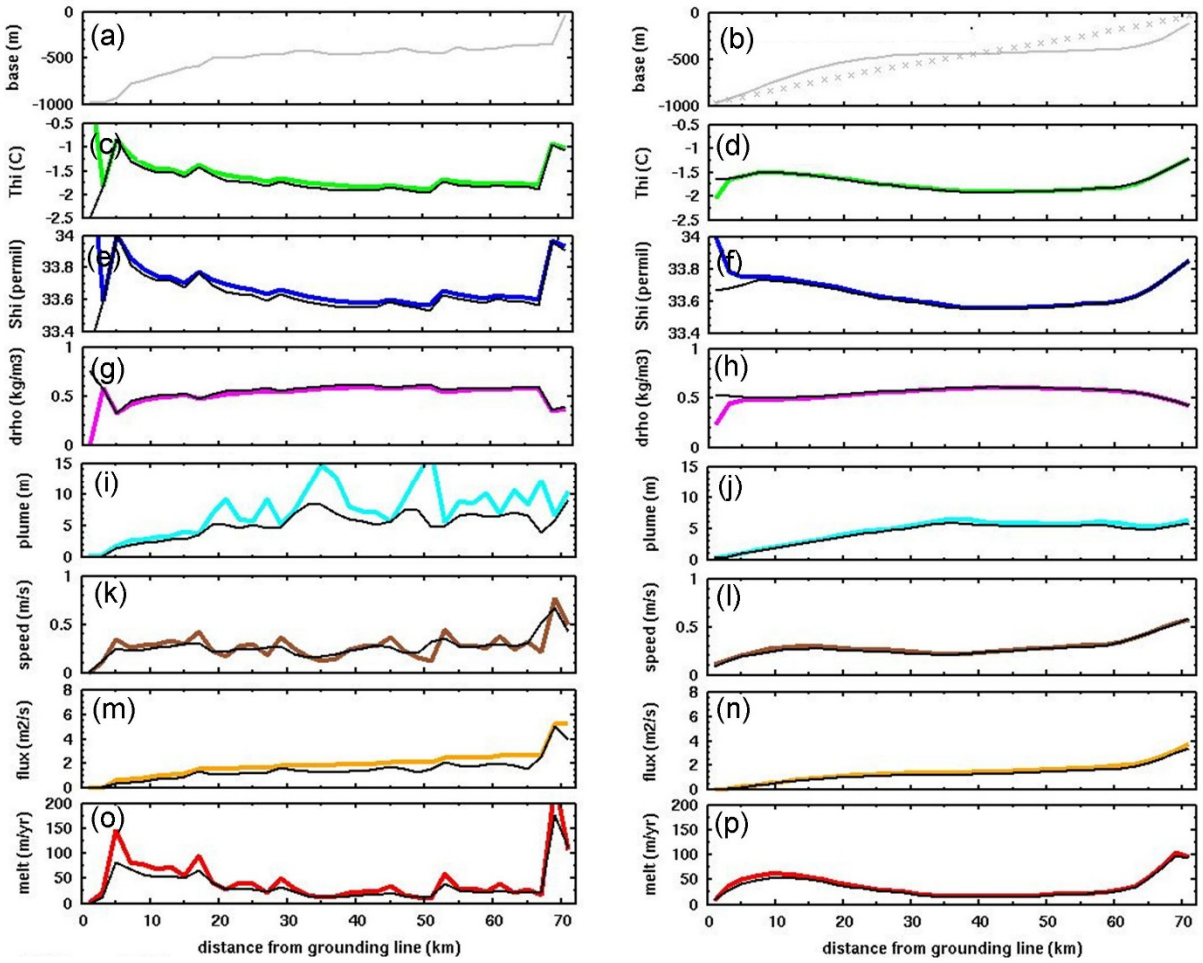

Figure S5.2. As Fig. S5.1 except for a profile along the approximate center line of Pine Island Glacier ice shelf, from grounding line to shelf edge. Thick colored lines are for the balance-flux model (Eqs. 4), and black lines are numerical solutions of the basic plume equations (Eqs. 1), both with grid resolution 2 km. Prescribed oceanic (and lower-layer) temperature T_o = 0.46 °C and salinity S_o = 34.55 ‰, as in Table 1 and Reese et al. (2018). **Left column:** No spatial smoothing applied to basal slopes sin α. **Right column:** Diffusive spatial smoothing applied to sin α for duration τ_{pig} = 0.1 years (Eq. 11). Quantities in panels a to p are as in Fig. S5.1. The basal ice depth in panel a is from Bedmachine (Morlighem, 2020; Morlighem et al., 2020) aggregated to our 2 km ASE grid, and smoothed with τ_{pig} = 0.1 yr in panel b. Crosses in panel b show an overly smoothed profile with τ_{pig} = 3 yr.

Again there is close agreement between the balance-flux model and the basic solutions, validating our numerical model procedures. The solutions for the profile without spatial smoothing (left-hand column) are noisy and respond to small-scale fluctuations in basal ice depth on scales of a few km (Fig. S5.2a). In this study we assume that the small-scale basal fluctuations are either not real, or are real but do not have important small-scale effects on cavity circulations and melt rates (but see Alley et al., 2019). The diffusive smoothing applied

for the right-hand column eliminates the small-scale noise but preserves the larger-scale shape of the profile (Fig. S5.2b), because with τ_{pig} = 0.1 years the effective length scale of diffusion (D_d τ_{pig})$^{1/2}$ is ~3 km. Longer durations of ~3 years or more produce too much smoothing and a close-to-linear basal profile (crosses in panel b).

References (also listed in main paper)

Adusumilli, S., Fricker, H. A., Medley, B., Padman, L., & Siegfried, M. R. (2020), Interannual variations in meltwater input to the Southern Ocean from Antarctic ice shelves. *Nature Geosc.*, https://doi.org/10.1038/s41561-020-0616-z.

Alley, K. E., Scambos, T. A., Alley, R. B., & Holschuh, N. (2019), Troughs developed in ice-stream shear margins precondition ice shelves for ocean-driven breakup. *Sci. Adv.*, 5, 10, eaax2215, doi: 10.1126/sciadv.aax2215.

Boyer, T.P., Baranova, O. K., Coleman, C., Garcia, H. E., Grodsky, A., Locarnini, R. A., Mishonov, A. V., Paver, C. R., Reagan, J. R., Seidov, D., Smolyar, I. V., Weathers, K. W., & Zweng, M.M. (2018), *World Ocean Database 2018*, NCEI, NOAA Atlas NESDIS 87, https://www.nodc.noaa.gov/OC5/WOD/pr_wod.html.

DeConto, R.M., & Pollard, D. (2016), Contribution of Antarctica to past and future sea-level rise. *Nature*, 531, 591-597.

Holland, P. R., Jenkins, A., & Holland, D. M. (2008), The response of ice shelf basal melting to variations in ocean temperature, *J. Clim.*, 21, 2558-2572.

Jenkins, A. (1991), A one-dimensional model of ice shelf-ocean interaction. *J. Geophys. Res.-Oceans*, 96, 20671-20677.

Morlighem, M. (2020), MEaSUREs BedMachine Antarctica, Version 2. Boulder, Colorado USA. *NASA National Snow and Ice Data Center Distributed Active Archive Center*. doi: https://doi.org/10.5067/E1QL9HFQ7A8M.

Morlighem, M., Rignot, E., Binder, T., Blankenship, D. D., Drews, R., Eagles, G., Eisen, O., Ferraccioli, F., Forsberg, R., Fretwell, P., Goel, V., Greenbaum, J. S., Gudmundsson, H., Guo, J., Helm, V., Hofstede, C., Howat, I., Humbert, A., Jokat, W., Karlsson, N. B., Lee, W., Matsuoka, K., Millan, R., Mouginot, J., Paden, J., Pattyn, F., Roberts, J. L., Rosier, S., Ruppel, A., Seroussi, H., Smith, E. C., Steinhage, D., Sun, B., van den Broeke, M. R., van Ommen, T., van Wessem, M., & Young, D. A. (2020), Deep glacial troughs and stabilizing ridges unveiled beneath the margins of the Antarctic ice sheet, *Nature Geoscience,* 13, 132-137. https://doi.org/10.1038/s41561-019-0510-8.

Jenkins, A. (2011), Convection-driven melting near the grounding lines of ice shelves and tidewater glaciers*. J. Phys. Oceanogr.*, 41, 2279-2294.

Moholdt, G., Padman, L., & Fricker, H. A. (2014)., Basal mass budget of Ross and Filchner-Ronne ice shelves, Antarctica, derived from Lagrangian analysis of ICESat altimetry, *J. Geophys. Res.-Earth,* 119, 2361-2380, https://doi.org/10.1002/2014JF003171.

Pelle, T., Morlighem, M., & Bondzio, J. H. (2019), Brief communication: PICOP, a new ocean melt parameterization under ice shelves combining PICO and a plume model. *The Cryo.,* 13, 1043-1049.

Reese, R., Albrecht, T., Mengel, M., Asay-Davis, X., & Winkelmann, R. (2018), Antarctic sub-shelf melt rates via PICO. *The Cryo.,* 12, 1969-1985.

Rignot, E., Jacobs, S., Mouginot, J., & Scheuchl, B. (2013), Ice-shelf melting around Antarctica, *Science*, 341, 266-270.